Tutorial: RTM image enhancement; bad models and mad physics

Ian F. Jones[1*], Marcin Kobylarski[1] and John Brittan[1]

Abstract

The final stage of a shot-based migration process is usually the imaging condition, which brings together elements of the upcoming and downgoing wavefield for each shot gather in order to form an image contribution. This procedure suffers limitations owing to the approximations made in representing the physics of the system, and in addition to that, the final summation of all shot contributions necessarily assumes that the subsurface parameter model was perfect, such that all image contributions align perfectly for summation (within a Fresnel zone), as well as ideally having recorded data that are noise free and adequately sampled. In this work, we assess the effect of unresolvable velocity error on the final image, and present a case study example of a technique for compensating for these errors via a localized phase alignment of each of the many thousands of elemental traces that can contribute to the final image.

Introduction

Regardless of the model-building procedure we employ, there will always be remnant error in our estimation of subsurface parameters: this is a basic tenet of inverse theory. With contemporary waveform inversion procedures, these errors may only be of a scale length of tens of metres, but they will still affect our ability to form a high-resolution image. As we move towards higher-resolution imaging, whether due to the contributions to bandwidth gained from deghosting or from high frequency RTM imaging, such small-scale parameter errors will inevitably limit the final resolution of the image.

There are several classes of error that affect the image. Firstly we have the physics of the problem. In any computational technique, we make simplifying assumptions concerning the physics involved in the process, and then need a tractable numerical technique to realize that physics. Most, if not all, contemporary imaging techniques assume an acoustic earth model (i.e., all rocks are fluids, and cannot support shear propagation), and the majority of imaging algorithms deployed for very complex geological environments use shot migration algorithms for two-way propagation (such as reverse-time migration: RTM; Hemon 1978, McMechan 1983; Whitmore 1983; Baysal et al., 1983). Typically, a convolutional imaging condition is used for RTM imaging (Claerbout, 1971). The limitations of the RTM method are well understood (Yoon et al., 2004; Schleicher et al., 2007; Arntsen et al., 2010; Leveille et al., 2011) and many workers have outlined techniques to compensate for the failings of the approximate physics employed. The techniques include interferometric imaging (Sava & Poliannikov, 2008), least squares migration (Schuster 1997; Nemeth et al., 1999), and deconvolutional and illumination compensated imaging conditions. More recently, some workers have moved to address the issue of residual model error via phase or trim-static alignment of individual image contributions ('optical stacking' or 'adaptive optics': e.g., Etgen et al., 2014a, b; Albertin and Zhang 2014; Jones et al., 2015). It is this aspect that we consider in this work.

In its simplest form, the convolutional imaging condition for two-way acoustic migration produces four image contributions, not all of which may be desirable. Consider a source wavefield S, with downgoing and upcoming components S_d and S_u, respectively and a back-propagated receiver wavefield R, with upcoming and downgoing components R_u and R_d.

The convolutional imaging condition for a shot record is formed by the superposition of the source and receiver wavefield products at all coincident times integrated over time:

$$\text{Image} = S * R = (S_d + S_u) * (R_d + R_u) = S_d * R_u + S_d * R_d + S_u * R_u + S_u * R_d \quad (1)$$

This is followed by summation of all shot contributions (e.g., Liu et al., 2011).

For a simple reflection from one-way propagating wavefields, say illuminating a flat reflector, only the first of these terms ($S_d * R_u$) would represent the desired physical image: the other three terms will be undesired crosstalk terms and are non-physical (Figure 1). Conversely, if we had an overhanging interface in a medium with significant vertical velocity gradients where both the source and receiver-side wavefields turned, then the image could be formed from these turning waves reflecting from the underside of the overhang: in this case the useful contribution would be formed from the terms ($S_u * R_d$). Alternatively, an image

[1] ION
[*] Corresponding author, E-mail: ian.jones@iongeo.com
DOI: 10.3997/1365-2397.2017007

of a steep event illuminated by a double bounce on the receiver-side would be formed from the terms (S_d * R_d). Hence, RTM has the benefit of being able to form an image from illumination along complex travel paths, but has the downside of producing all combinations of the wavefields even when they don't physically exist, i.e. the crosstalk noise problem.

Whereas from the theoretical standpoint we should be dividing the upcoming by the downgoing wavefields (a deconvolutional imaging condition, see for example Jones 2014), here we are forming the image by the product of the downgoing and upcoming wavefields, and then normalizing this product to emulate the desired division. In other words: approximating the desired division via a convenient, more stable, multiplication ('mad physics'). This normalization is referred to as illumination compensation (e.g., Schleicher et al., 2007; Liu et al., 2011).

We can try to form this imaging condition more correctly with a form of inversion or deconvolution (a least-squares or deconvolutional imaging condition, e.g., Schuster 1997; Nemeth et al., 1999; Guiton et al., 2006), or separation of the pertinent upcoming and downgoing terms during migration (e.g., Xia and Rietveld, 2013; Yoon and Marfurt, 2006), but these methods tend to be expensive, so are not currently in widespread industrial use. The convolutional procedure described above results in various artefacts in the RTM image: in other words, the results of 'mad' physics.

In addition, and/or alternatively, we can try to suppress the resulting artefacts on the final image or in gathers created via a modified imaging condition (e.g., Sava and Fomel 2003, 2006; Fletcher et al., 2005; Xu et al., 2010; Kaelin and Carvajal, 2011; Zhang and McMechan, 2011; Xie et al., 2012; Zhou et al., 2011). The nature of the main class of artefact formation is shown in Figure 1, and for a field data example in Figure 2 (from Jones and Davison, 2014). In Figure 2a, the low-frequency background 'image condition' noise is seen in most places above the point where the critical angle is reached for either the downgoing or upcoming wavefields. After suppression of the noise with a Laplacean filter (Figure 2b) we can still see a pernicious class of near-vertical artefact (indicated by the yellow arrow) which occurs where there is significant lateral velocity change within a Fresnel zone scale length (because the multiplicative convolutional imaging condition is inappropriate: another manifestation of bad physics). This class of noise can be removed by filtering angle gathers (Figure 2c).

However, once we have produced a clean image and gathers, we still face the problem of resolution degradation owing to unresolved (and unresolvable) velocity error (e.g., Jones, 2010). Consequently, the final integral used to form the image, namely over each shot contribution, will suffer from image misalignment because of these small-scale velocity errors in the migration velocity model. It is a compensation scheme for these latter effects that are the subject of the remainder of this paper.

Methodology and synthetic examples

Consider the contribution to an image from a single shot gather for a simple salt diapir model. Figure 3a shows the downgoing source wavefield (in black and red) superimposed on the upcoming receiver wavefield (in grey and white) for propagation time

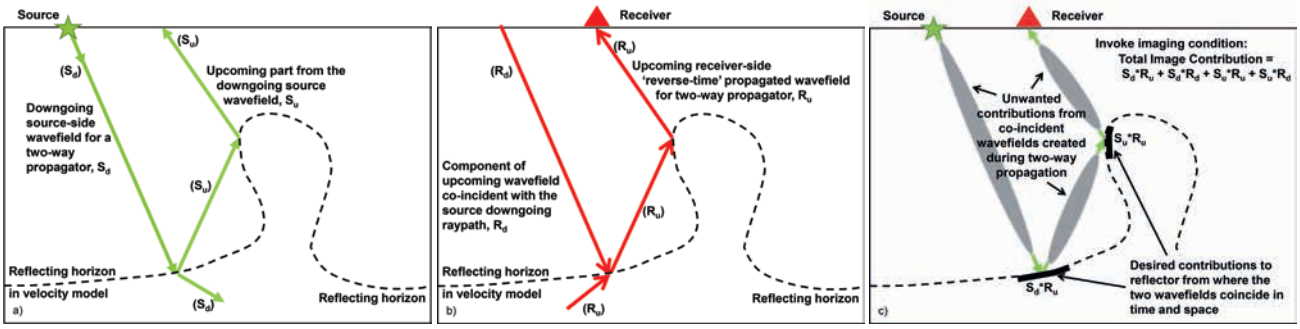

Figure 1 Two-way shot migration imaging condition for an overhanging reflector. a) Downgoing source-side wavefield for two-way propagation – this has energy on the downgoing path, S_d, but also creates a contribution back up along the upcoming path, S_u. b) Upcoming receiver-side wavefield, R_u, propagated back into the earth towards the reflector (hence the name 'reverse-time'). The propagation algorithm also reflects this wavefield back upwards towards the source, R_d. c) Imaging condition from multiplying both wavefields together to form a contribution to the final image, but we also get an unwanted image contribution that has to be removed (the grey regions along coincident portions of the ray paths).

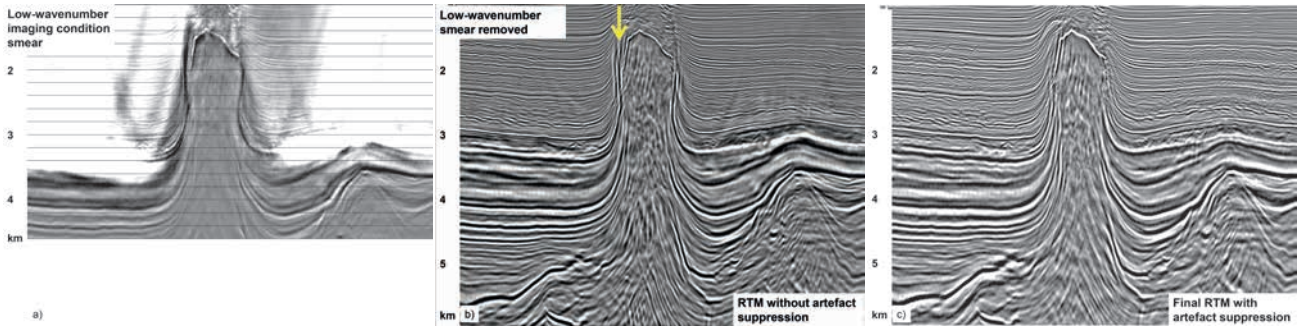

Figure 2 a) Shallow section from the RTM image prior to filtering the backscattered noise; b) Deeper section showing near vertical RTM artefact emanating from a strong reflector termination (indicated with the yellow arrow). This image is taken from an early stage of the velocity model building. c) Image from later stage in the model building after filtering of RTM angle gathers (From Jones and Davison, 2014: ION RTM image shown courtesy of Talisman Sinopec Energy UK and partners GdF-Suez, EON and Idemitsu. Input data courtesy of CGG).

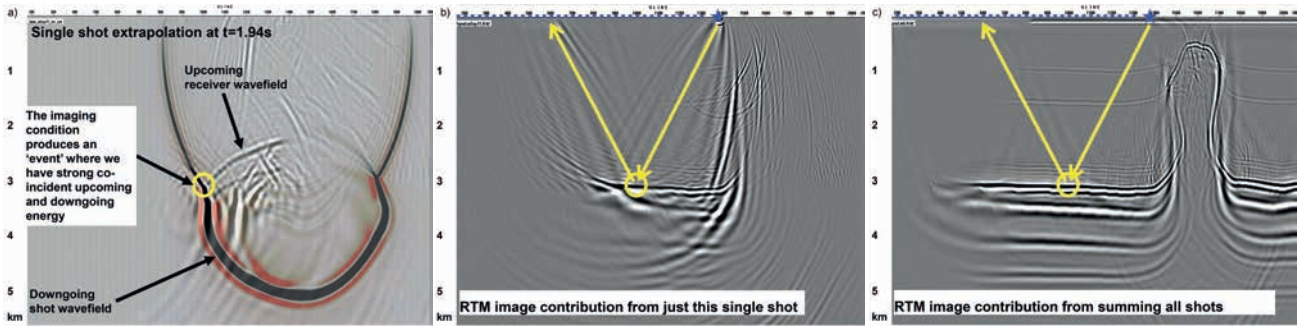

Figure 3 a) upcoming and downgoing wavefields at time = 1.94 s. b) Image contribution from migrating a single shot gather (i.e. the source and receiver products for all propagation times have been summed). c) Final RTM image after addition of the migrations of all contributing shots. The yellow circle in the three images indicates the same point in space, showing how the image of this point is built up in the overall procedure.

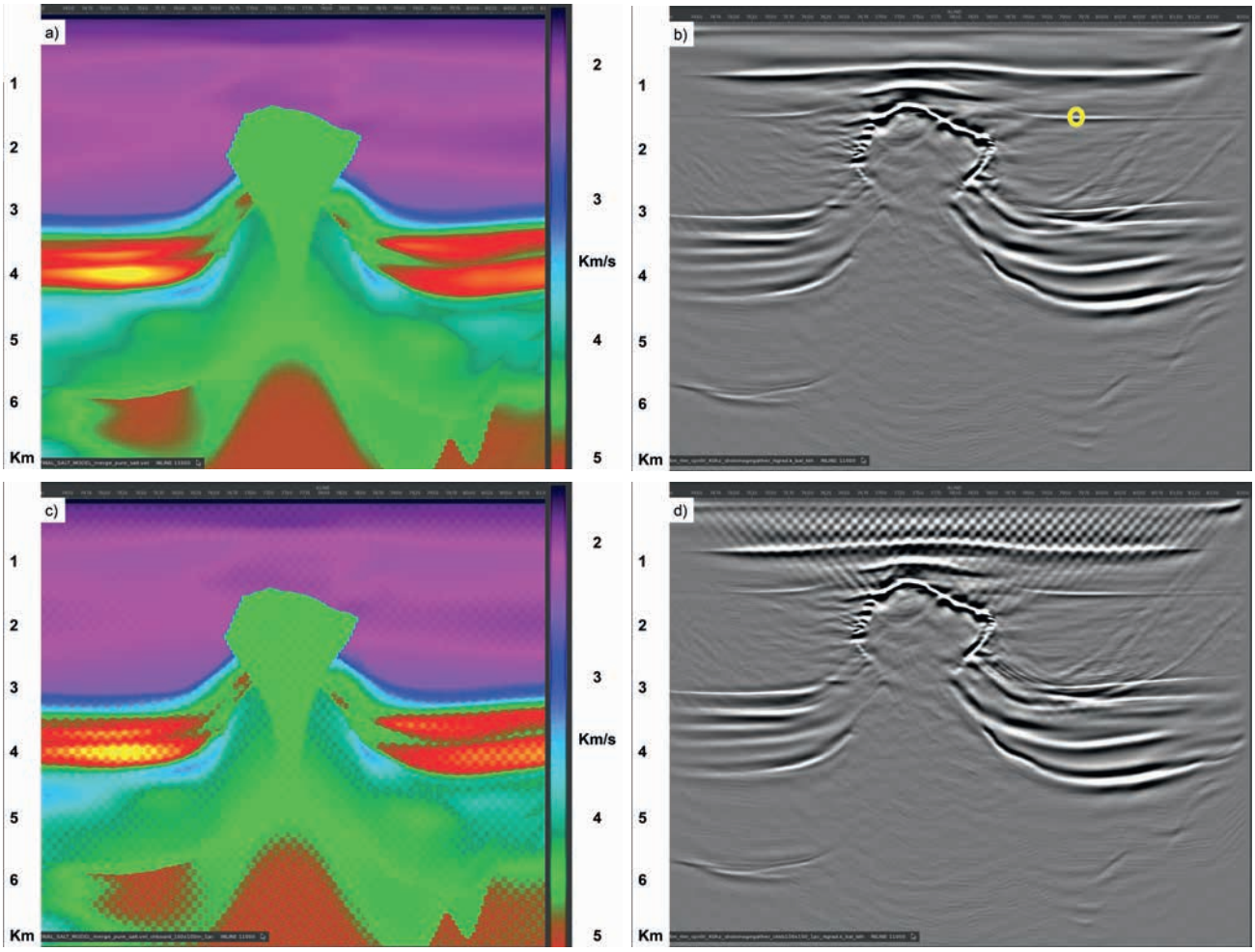

Figure 4 a) model used to create synthetic shot gathers. b) RTM using the correct model. c) Model with a ±1% interval velocity perturbation on a 100 m *100 m grid (the yellow circle indicates the location of the elemental gather shown later). d) RTM image formed using the perturbed model.

1.94 s. The product of these two wavefields constitutes the image contribution for this propagation time, and the final migrated contribution for this shot would be formed from the sum of this product over all propagation times, as shown in Figure 3b. The convolutional imaging condition has produced an image of the flat reflector for CMP locations ranging from between the shot location and the first receiver, all the way out to a location half way along the spread length. On either side of the correctly imaged flat reflector segment, we have a portion of migration response noise. Summing over all shots creates the final image, shown in Figure 3c. At this stage, most of the migration noise and image artefacts have cancelled-out, producing an acceptable subsurface image. The yellow circle on each of the three images is a common point indicating the production of the image contribution (3a), its position in the partial image contribution from a single shot's migration (3b) and in the final fully migrated image after all shot contributions have been summed (3c).

If we were now to consider just one surface location and collect all the individual shot contributions to this point, we would have what we refer to as an elemental contribution gather.

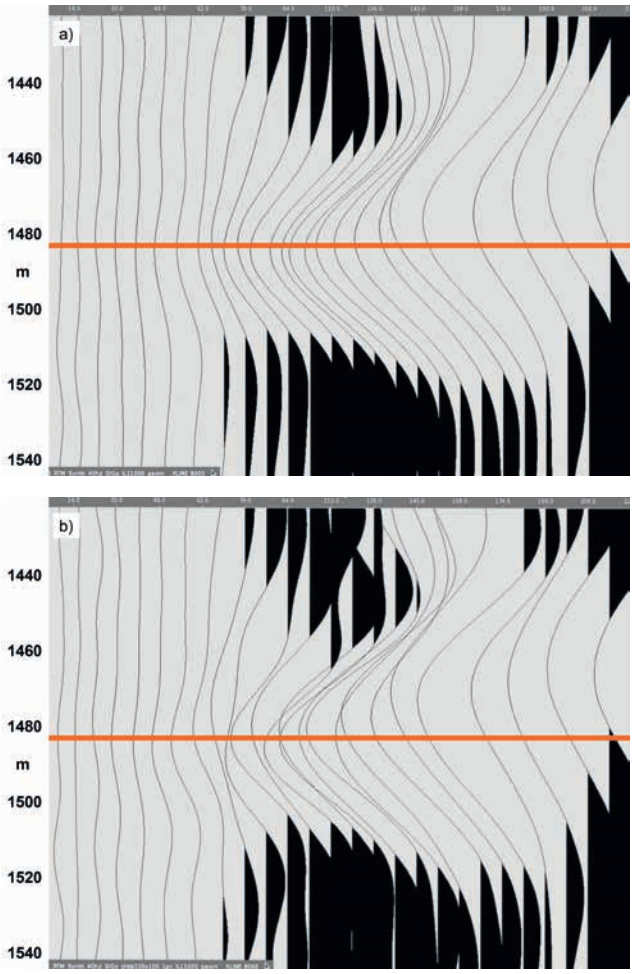

Figure 5 a) The twenty-five most energetic traces extracted from the elemental contribution gather from migration using the correct model for a shallow flat-lying reflector indicated by the yellow circle in Figure 4c. The central portion of the gather shows flat-lying events which will sum to form the image: at the edges of the flat region, we have migration impulse response noise curling upwards. b) Traces from the elemental contribution gather resulting from RTM using the perturbed model. The trace-to-trace a jitter in the elemental contribution gather from the perturbed model migration is about ± 10 m.

Many of these contributions are useful signals (namely those that fall within a Fresnel zone of the image point), but most will be migration noise (i.e. non-physical numerical noise resulting from a combination of the shot and receiver extrapolations and subsequent imaging condition). Usually the contributions to the image from individual shots are summed 'on the fly' or at best in shot-offset-azimuth tiles, so as to suppress unwanted migration noise (Xia and Rietveld 2013; Tyson et al., 2015).

As a separate issue from the migration noise problem, we can assess the effect of model error ('bad models') on these image contribution gathers by migrating synthetic data with and without model error. To assess the effect on an elemental gather of velocity model errors, we have perturbed the model used to create the data with a checkerboard pattern with a cell size of 100*100m, and velocity perturbations of ±1%. These small-scale velocity perturbations are taken to be representative of the degree of velocity uncertainty likely to be present after a comprehensive model building exercise. Figure 4a and 4b show the velocity model used to create the synthetic shot gathers and an RTM image using the correct model. Figures 4c and 4d show the model after perturbation and the associated RTM image. As expected, with these small velocity errors there is very little visible image degradation, apart from in the very shallow part of the image.

After migrating with the correct model, the image contribution gather is flat for reflectors within a Fresnel zone (Figure 5a), where events would sum to form the final image. However, for RTM using the perturbed model, we can see that the hitherto flat central portion of the gather now has a trace-to-trace jitter of about ± 10 m (Figure 5b). This jitter and general distortion of the waveform, results from the small-scale velocity errors introduced into the migration model. In a real tomographic (and/or FWI) iterative model updating project, we would expect there to always be some residual (and more importantly – unresolvable) velocity error in our final model (note that the unresolvable components of the model error, manifest as jitter on the elemental gathers, will still be present even if the CRP gathers output from the migration were all flat). However, we should be able to ameliorate the resulting image degradation by performing localized wavelet shaping and alignment of these jittering traces in a sliding window, using a pilot stacked trace as a reference function, and then limiting the subsequent summation of aligned elemental waveforms to within a Fresnel zone. In this way, we could recover some of the potential image resolution lost due to both the unresolvable model error and any observable remnant model error (non-flat gathers) remaining after iterative model update.

Results for a field data example

Here we consider data from an offshore shallow water environment (courtesy of Harvest Natural Resources) where we have a complex salt canopy below a very high velocity carbonate layer: so here the salt is the low-velocity medium (Pavlov et al., 2016). Figure 6a shows the final RTM image from the production project with a colour overlay of the interval velocity model. The rugose dark-green region between 2km and 3km depth is the salt body.

For these data, we have several thousand migrated shot gather contributions in each of the elemental gathers being summed to form the final image. Figure 7 shows the basic 45 Hz RTM output

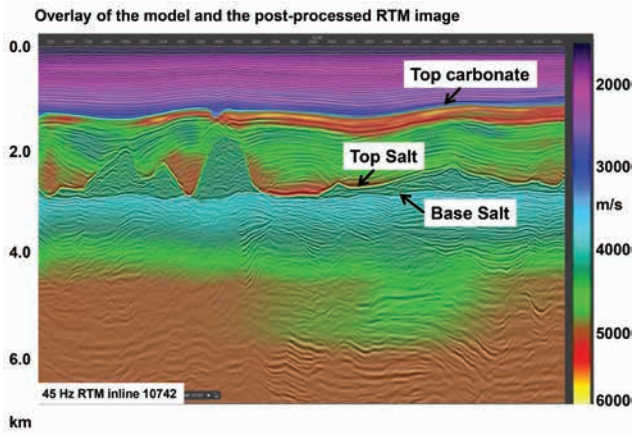

Figure 6 interval velocity model overlay on image after tomographic inversion of residual moveout as picked from the angle gathers for sub-salt events. Shallow-water Gabon example, courtesy of Harvest Natural Resources and Panoro Energy.

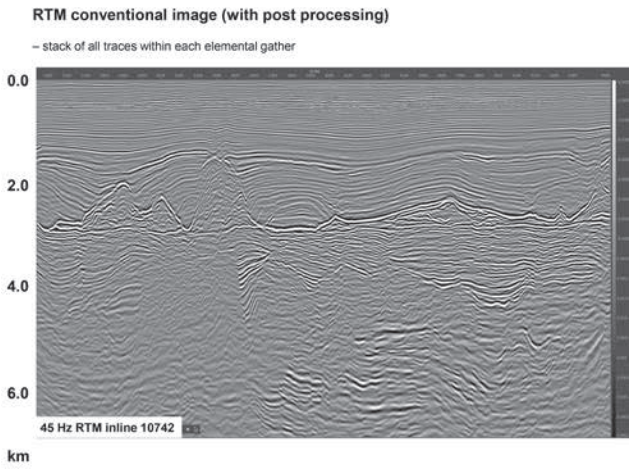

Figure 7 Simple stack of all migrated shot contributions, after basic post-processing.

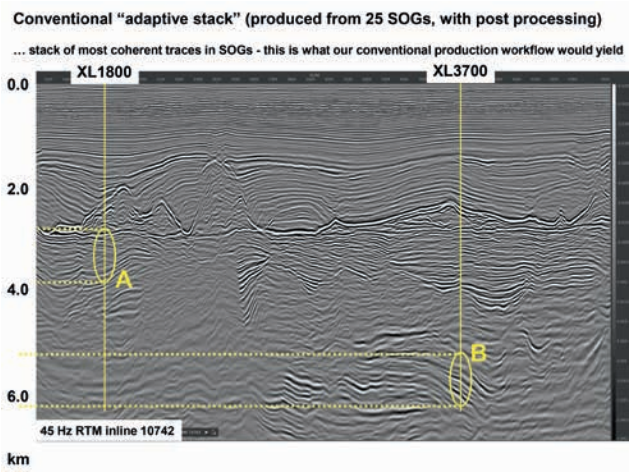

Figure 8 Enhanced stack using 25-fold shot offset-azimuth image gather tiles (SOGs) with coherency weighting to a pilot trace in sliding windows. Much of the background noise is suppressed. Two yellow ellipses are indicated on the figure, one near the base salt reflector and one on a deeper event: elemental image contribution gathers for these locations will be shown next.

from migrating these shot gathers (after some rudimentary image processing to remove RTM noise). This image can be readily improved by performing enhanced coherency-weighted stacking of offset and azimuth partitioned image contributions (Xia and Rietveld 2013; Tyson et al., 2014). Figure 8 shows the corresponding image formed from the input shot gathers following partition into 25 offset-azimuth classes, and coherency-weighted stacking of the most similar contributions from the 25-fold image partitioned gathers.

Here we extend the notion of the offset-azimuth tiled coherency-weighted stack by retaining all of the individual image contributions, the elemental gathers (i.e. not sub-stacked into 25 tiles), and furthermore, attempt to enhance image resolution by phase aligning all image contribution traces in a sliding depth window prior to coherency-weighted stacking. The depth variant phase alignment is accomplished using a wave shaping filter in sliding windows, where each trace is compared to a pilot stack. After the phase alignment, we again perform an enhanced stack wherein each of the aligned elemental traces in the gather are compared to a pilot trace and weighted in accordance to similarity with the pilot in a sliding window.

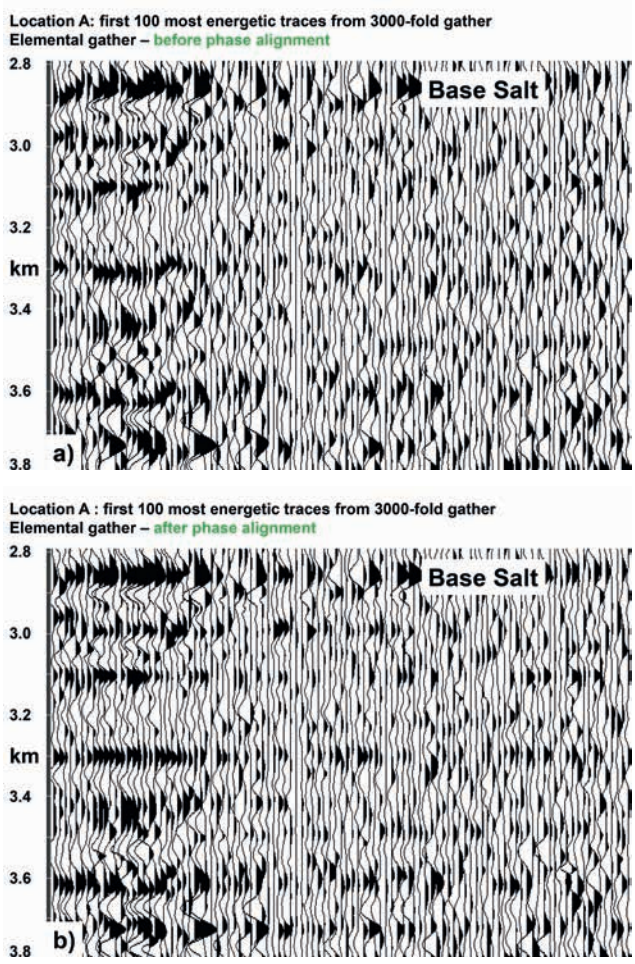

Figure 9 Location A. The first 100 most energetic traces from the possible thousands of traces in the elemental gather at the base-salt reflector (a) before and (b) after phase alignment.

Now consider the location 'A', indicated in Figure 8, and look at the elemental image contribution gathers for the base-salt event. In this case, the 3D swath of input field data used to form this particular output imaged line comprised thousands of shot gathers, hence the image contribution gather is of many-thousand fold. In Figure 9, only the first 100 most energetic traces from the thousands of possible traces in the elemental gather are shown for a small vertical window at the base of salt, before and after phase alignment. In the display, traces are sorted in terms of energy content at the base salt reflector (rather than say offset or azimuth). From Figure 9a we can see a trace-to-trace jitter of about ±20 m on signal wavelengths of about 80 m, which is mostly removed after the phase adjusted windowed alignment (Figure 9b). Figure 10 shows the corresponding adaptive stacks of the two sets of gathers, showing an overall increase in stack amplitude. The vertical line at cross-line 1800 denotes where the elemental gather in Figure 9 is located.

Assessing the alignment results for a sub-salt reflector (location 'B', at about 5500 m in Figure 8), we have the elemental gathers seen in Figure 11 for the unaligned data (11a), and phase aligned data (11b). Here, the jitter in the conventional elemental gather is about ±30 m, and being deeper in the section, the waveforms are of greater wavelength – about 150 m (owing to both velocity dependent stretch and absorption of higher frequencies).

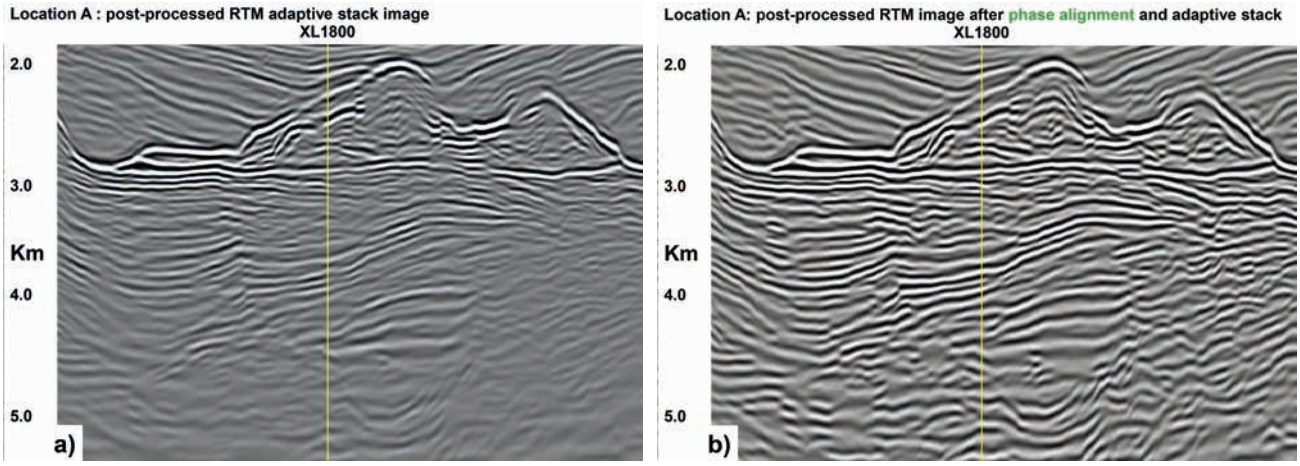

Figure 10 Location A. a) Coherency-weighted enhanced-stack of 25-fold SOGs, b) Coherency-weighted enhanced -stack of phase-aligned gathers. In places the stack amplitude is almost doubled, and overall the reflector strength and resolution are increased. Unsurprisingly, in some areas, noise is also enhanced. But overall, the image improvement is significant.

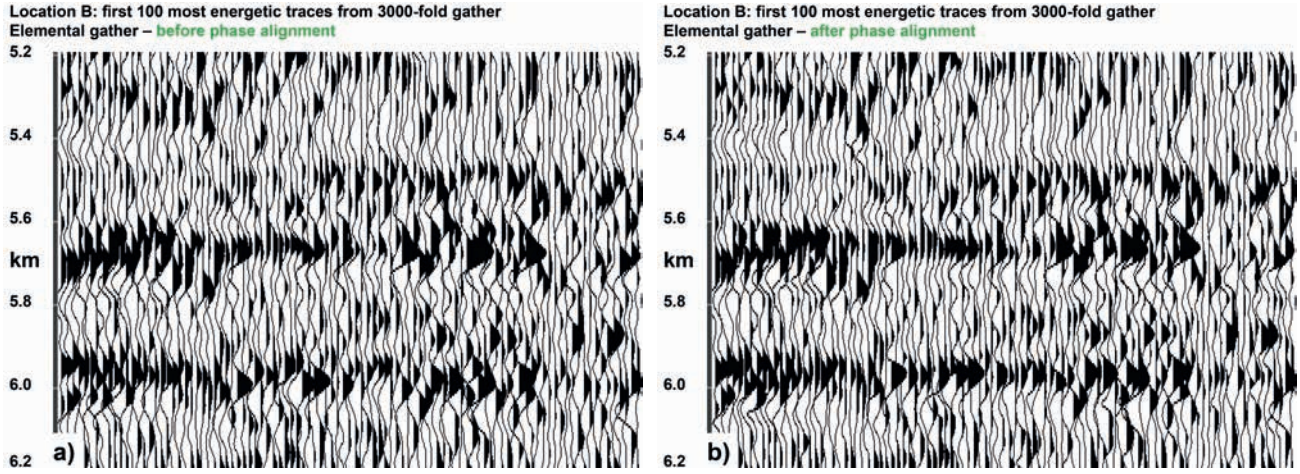

Figure 11 Location B. The first 100 most energetic traces from the possible thousands of traces in the elemental gather at the deeper sub-salt reflector (a) before and (b) after alignment

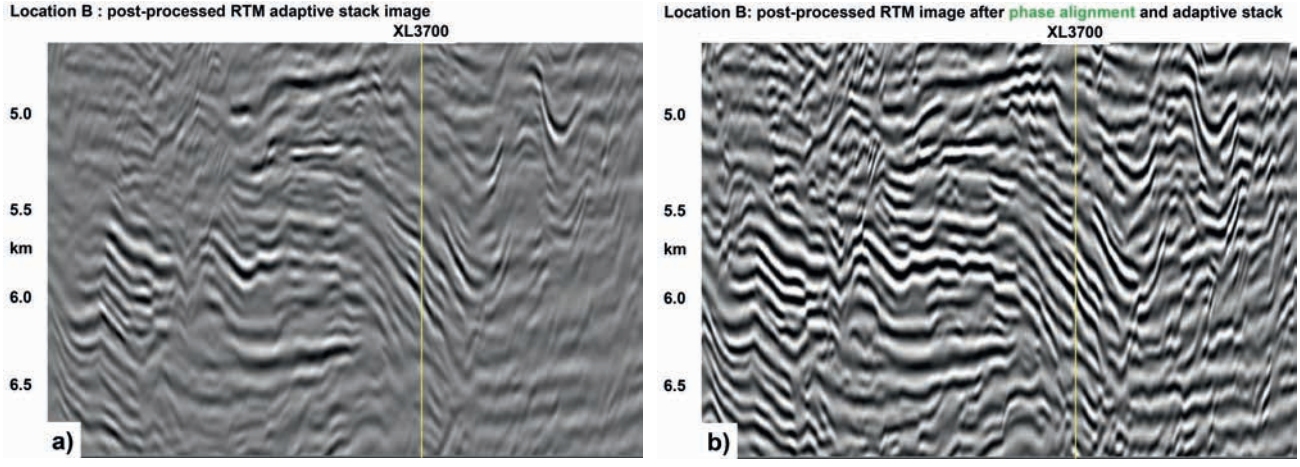

Figure 12 Location B. a) Adaptive-stack of 25-fold SOGs, b) Adaptive-stack of phase-aligned gathers. In places the stack amplitude is almost doubled, and overall the reflector strength and resolution are increased.

Comparing Figures 10a and 10b, and also 12a and 12b, we note that in places the amplitude of events is more than doubled. A simple increase in overall amplitude could be obtained with application sliding window gain (AGC), but an AGC cannot improve the signal bandwidth. Conversely, and as expected, the phase alignment procedure improves the bandwidth in the ensuing signal after stacking, as we have circumvented unnecessary destructive interference of misaligned signal energy (by about 8 dB at frequency 20 Hz) as shown in Figure 13.

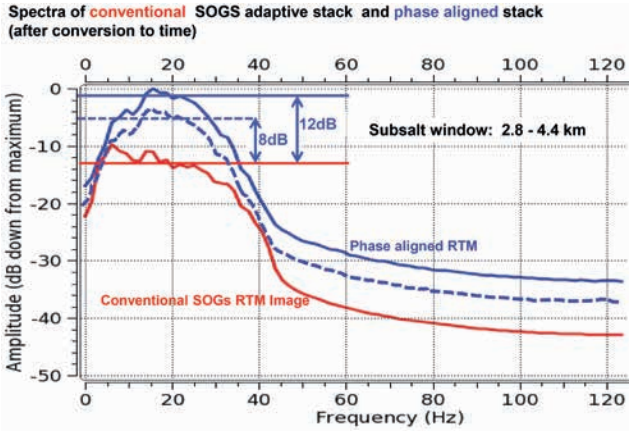

Figure 13 Amplitude spectra of the images in Figures 10a and 10b, after conversion to time. Between about 5 Hz-35 Hz the signal strength is boosted by about 8 dB, giving a broader signal bandwidth. The red curve is the spectrum of the conventional image and the solid blue curve is that of the phase adjusted image (sitting some 12 dB above the conventional data spectrum). However, given that the phase adaptation procedure will inevitably increase noise, we have manually adjusted the spectrum (dashed blue curve) to align it with the conventional result at about 5 Hz, as here the signal is likely to be more dominant, thus giving a more realistic indication of signal strength improvement

Discussion

It is well known that the imaging conditions used for RTM give rise to artefacts that can be ameliorated via various pre and post-stack signal processing techniques. However, perhaps of more concern is the effect of image degradation resulting from unresolved and unresolvable velocity error. Velocity errors of a scale length comparable to the wavelength of the seismic energy being used to illuminate the subsurface can significantly limit the resolution available to the observer.

Assessing and compensating for these small errors can facilitate enhancing the images obtained during conventional RTM so as to extract the maximum amount of information available from the computational effort. However, to do this requires modification of the latter stages of the imaging process: namely the final integration over each shot migration's contribution to the image. Although it might not yet be practical to store all the many thousands of individual elemental image contributions for post-processing, computational methods can be employed to improve the image by comparing elemental contributions to a pilot image without excessive data storage.

Unsurprisingly, the technique as presented does run the risk of enhancing remnant multiples and other coherent noise. For Kirchhoff and beam techniques, we routinely apply residual multiple suppression on the migrated CRP gathers to avoid contaminating the final image, and a similar procedure could be adopted here. To achieve this, the phase alignment and coherency weighted stacking could be performed in offset and azimuth subsets, so as to create sub-stacked gathers appropriate for treatment with Radon (or other) multiple suppression techniques.

Acknowledgements

Our sincere thanks goes to Nick Bernitsas, Dave McCann, and Jacques Leveille, and to the FB reviewer for helpful suggestions for improvement of this work. Thanks also to Talisman Sinopec Energy UK and partners GdF-Suez, EON, and Idemitsu (and data owners CGG), for use of the North Sea salt diaper example, as well as to Harvest Natural Resources and Panoro Energy for permission to show the Gabon example, and to ION for permission to publish.

References

Albertin U. and Zhang, L. [2014]. Migration optimization through local phase alignment of partial migration images. *SEG Technical Program,* Expanded Abstracts, 3769-3773.

Arntsen, B., Tantserev, E. and Amundsen, L. [2010]. True-amplitude cross-correlation shot-profile imaging condition. *SEG Technical Program,* Expanded Abstracts, 3273-3277.

Baysal, E., Kosloff, D.D. and Sherwood, J.W.C. [1983]. Reverse time migration: *Geophysics*, **48**, 1514-1524.

Claerbout, J. F. [1971]. Toward a unified theory of reflector mapping. *Geophysics*, **36**, (3), 467-481.

Etgen, J.T., Chu, C., Yang, T. and Vyas, M. [2014a]. Adaptive image focusing. *SEG Technical Program,* Expanded Abstracts, 3774-3778.

Etgen, J.T., Ahmed, I. and Zhou, M. [2014b]. Seismic adaptive optics. *SEG Technical Program,* Expanded Abstracts, 4411-4415.

Fletcher, R.F., Fowler, P., Kitchenside, P. and Albertin, U. [2005]. Suppressing artefacts in prestack reverse-time migration. *SEG Technical Program,* Expanded Abstracts, 2049–2051.

Guitton, A., Kaelin, B. and Biondi, B. [2006] Least-square attenuation of reverse-time migration artefacts. *SEG Technical Program,* Expanded Abstracts, 2348–2352.

Hemon, C. [1978]. Equations d'onde et modeles. *Geophysical Prospecting*, **26**, 790–821.

Jones, I.F. [2010]. *An introduction to velocity model building*. EAGE Publications, Houten, The Netherlands.

Jones, I.F. [2014]. Tutorial: migration imaging conditions. *First Break*, **32**, no.12, 45-55.

Jones, I.F and Davison, I. [2014]. Seismic imaging in and around salt bodies. *Interpretation*, **2**, no.4, SL1-SL20.

Jones, I.F., Kobylarski, M. and Brittan J. [2015]. An overview of some wavefield extrapolation imaging conditions. *SEG Technical Program,* Expanded Abstracts.

Kaelin, B. and Carvajal, C. [2011]. Eliminating imaging artifacts in RTM using pre-stack gathers. *SEG Technical Program,* Expanded Abstracts.

Leveille, J.P., Jones, I.F., Zhou, Z-Z., Wang, B. and Liu, F. [2011]. Subsalt imaging for exploration, production and development: A review. *Geophysics*, **76**, (5), WB3– WB20.

Liu, F., Zhang, G., Morton, S.A. and Leveille, J.P. [2011]. An effective imaging condition for reverse-time migration using wavefield decomposition. *Geophysics*, **76**, S29–S39.

McMechan, G.A. [1983]. Migration by extrapolation of time-dependent boundary values. *Geophysical Prospecting*, **31**, 413-420.

Nemeth, T., Wu, C. and Schuster, G.T. [1999]. Least-squares migration of incomplete reflection data. *Geophysics*, **64**, 208-22.

Pavlov, A., Fruehn, J., Sugrue, M., Cox, B. and John Price, J. [2016]. Third time lucky? Imaging the Dentale formation offshore Gabon. *78th EAGE Conference & Exhibition*, Extended Abstracts.

Sava, P. and Fomel, S. [2003]. Angle-domain common-image gathers by wavefield continuation methods. *Geophysics*, **68**, 1065-1074.

Sava, P. and Fomel, S. [2006]. Time-shift imaging condition in seismic migration. *Geophysics*, **71**, S209-S218.

Sava, P. and Poliannikov, O. [2008]. Interferometric imaging condition. *Geophysics*, **73**, S47–S61.

Schleicher, J., Costa, J.C. and Novais, A. [2007]. *A Comparison of Imaging Conditions for Wave-Equation Shot-Profile Migration*. Accessed online, October 2015, at: http://www.portalabpg.org.br/PDPetro/4/resumos/4PDPETRO_1_2_0533-1.pdf.

Schuster, G. [1997]. Acquisition footprint removal by least square migration. *1997 Annual UTAM Report*, 73-99.

Tyson, C., Kobylarski, M., Walters, R. and Long, S. [2015]. Sub-salt model update and RTM image enhancement: an example from deep water Angola. *75th EAGE Conference & Exhibition*, Extended Abstracts.

Whitmore, N.D. [1983]. Iterative depth migration by backward time propagation: 53rd Annual International Meeting. *SEG Technical Program,* Expanded Abstracts.

Xia, G. and Rietveld, W. [2013]. Aperture Partitioned Illumination and Weighting for Optimized Subsalt Imaging. *75th EAGE Conference & Exhibition*, Extended Abstracts.

Xie, J., Whiteside, W. and Wang, B. [2012]. Remove RTM Artifacts Using Delayed Imaging Time Gathers. *SEG Technical Program,* Expanded Abstracts.

Xu, S., Zhang, Y. and Tang, B. [2010]. 3D common image gathers from reverse time migration. *SEG Technical Program,* Expanded Abstracts, 3257–3262.

Yoon, K., Marfurt, K.J. and Starr, W. [2004]. Challenges in reverse-time migration. *SEG Technical Program,* Expanded Abstracts, 1057–1060.

Yoon, K. and Marfurt, K.J. [2006]. Reverse-time migration using the Poynting vector. *Exploration Geophysics*, **37**, 102–107.

Zhang, Q. and McMechan, G.A. [2011]. Direct vector-field method to obtain angle -domain common image gathers for isotropic acoustic and elastic reverse-time migration. *Geophysics*, **76**, WB135–WB149.

Zhou, Z.Z., Howard, M. and Mifflin, C. [2011]. Use of RTM full 3D subsurface angle gathers for subsalt velocity update and image optimization: Case study at Shenzi field. *Geophysics*, **76**, WB27–WB39.